# Preserving Charge and Oxidation State of Au(III) Ions in an Agent-Functionalized Nanocrystal Model System

**Stefan Müllegger,[†,*] Wolfgang Schöfberger,[‡] Mohammad Rashidi,[†] Thomas Lengauer,[†] Florian Klappenberger,[¶] Katharina Diller,[¶] Kamuran Kara,[¶] Johannes V. Barth,[¶] Eva Rauls,[§] Wolf Gero Schmidt,[§] and Reinhold Koch[†]**

[†]Institute of Semiconductor and Solid State Physics and [‡]Institute of Inorganic Chemistry, Centre for Nanobionics and Photochemical Sciences (CNPS), Johannes Kepler University, 4040 Linz, Austria, [¶]Physik-Department E20, TU München, 85748 Garching, Germany, and [§]Lehrstuhl für Theoretische Physik, Universität Paderborn, 33098 Paderborn, Germany

**ABSTRACT** Supporting functional molecules on crystal facets is an established technique in nanotechnology. To preserve the original activity of ionic metallorganic agents on a supporting template, conservation of the charge and oxidation state of the active center is indispensable. We present a model system of a metallorganic agent that, indeed, fulfills this design criterion on a technologically relevant metal support with potential impact on Au(III)-porphyrin-functionalized nanoparticles for an improved anticancer-drug delivery. Employing scanning tunneling microscopy and -spectroscopy in combination with photoemission spectroscopy, we clarify at the single-molecule level the underlying mechanisms of this exceptional adsorption mode. It is based on the balance between a high-energy oxidation state and an electrostatic screening-response of the surface (image charge). Modeling with first principles methods reveals submolecular details of the metal–ligand bonding interaction and completes the study by providing an illustrative electrostatic model relevant for ionic metalorganic agent molecules, in general.

**KEYWORDS:** gold(III) · porphyrin · frontier orbitals · functional · nanotemplate · oxidation state stabilization · STM

Porphyrins can stabilize $Au^{III}$ ions in solution,[1] thus acting as efficient electron acceptors and making them efficient catalysts[2,3] as well as highly potent medical agents with specific antitumor and anti-HIV activity.[4−8] The photonuclease activity of water-soluble $Au^{III}$ porphyrins for sequence-specific catalytic DNA cleavage, for instance, has recently been demonstrated.[8,9] To minimize damage of nontumor cells, a targeted drug delivery in the body is desirable. An increasingly attractive carrier system for therapeutical agents[10,11] and biomarkers[12] are nanoparticles providing well-defined facet surfaces for the functionalization with agent molecules. In particular, the functionalization of gold nanoparticles with porphyrins has been recently realized.[11,13] For a successful functionality control the stabilization of the desired reactive state and accessibility of the frontier orbitals of the active center are of utmost importance, necessitating an appropriate interaction between the agent and its support.

As pointed out in a recent *in vitro* study by Lum *et al.*,[14] $Au^{III}$-tetraphenylporphyrin (AuTPP) is an effective, physiologically stable antitumor agent. First hints on a conservation of the required active Au(III) state of AuTPP in contact with a gold template by Müllegger *et al.*[15] are a promising starting point for the development of a nanoparticle-supported agent system tailored to an improved selective drug delivery. Here we report on a single-molecule study of $[Au^{III}TPP]^+Cl^-$ on Au(111) as a model system for nanoparticle-supported drug delivery and demonstrate that main design criteria are fulfilled. (i) The $Au^{III}$ oxidation state of AuTPP relevant for the antitumor activity is preserved on Au(111) facets. (ii) The charge state of the $[Au^{III}TPP]^+$ cation leads to a negative image charge in the conducting template, which can be utilized to shift the chemically active d orbitals of the Au center to desired energy levels, and thereby, making them active or inactive. The presented experimental and theoretical results provide mechanistic insight into fundamental atomistic processes, resulting in an interaction scheme with relevance for supported ionic metalorganic agents, in general, comprising an active metal ion center with differently stable oxidation states.

## RESULTS AND DISCUSSION

**Verifying $[Au^{III}(TPP)]^+$ Cations on Au(111) Facets.** The low-temperature (LT) scanning tunneling microscopy (STM) topograph of Figure 1a shows the sample surface at 7 K after room-temperature deposition of our model agent molecule, $Au^{III}$ 5,10,15,20-meso-tetraphenylporphyrin chloride ($[Au^{III}(TPP)]^+Cl^-$). Two different adsorbate species labeled 1 and 2, both

* Address correspondence to stefan.muellegger@jku.at.

Received for review May 10, 2011 and accepted July 7, 2011.

**Published online July 07, 2011**
**10.1021/nn201708c**

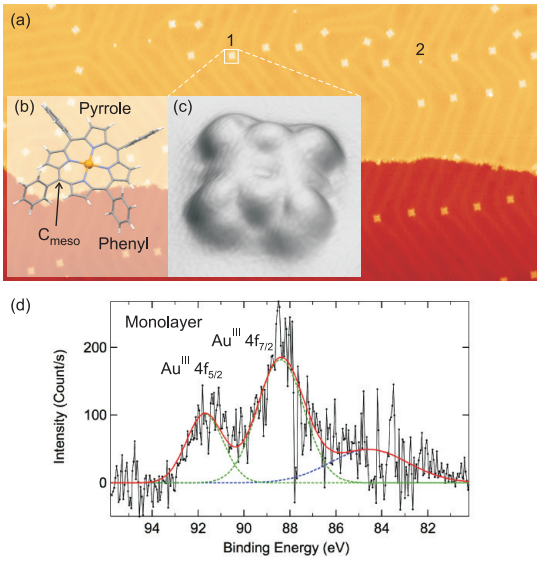


**Figure 1. (a) LT-STM topograph of a Au(111) facet after room temperature deposition of $[Au^{III}(TPP)]^+$ $Cl^-$ (130 × 65 nm², +1 V, 30 pA) revealing two different species labeled 1 ($[Au^{III}(TPP)]^+$) and 2 (chlorine). (b) Chemical structure of $[Au^{III}(TPP)]^+$. (c) Three-dimensional view of high-resolution STM image of a single $[Au^{III}(TPP)]^+$ (+50 meV, 10 pA). (d) XPS spectrum of the Au 4f region of a monolayer of $Au^{III}TPP^+$ on Au(111) obtained after subtracting the scaled signal of a freshly cleaned Au(111) surface; the $Au^{III}$ 4f doublet lies at 88.4 and 91.7 eV; the broad single peak centered at 84.5 eV is a residual structure from the subtraction procedure.**

not detected on the pristine substrate, are clearly observed. The first species is adsorbed atop Au herringbone elbows and is easily identified as single AuTPP molecules by their characteristic size, shape, and intramolecular features (see Figure 1c).[15,16] No topographic evidence for a $Cl^-$ counterion attached to individual AuTPP moieties is found by STM, in accordance with our X-ray photoemission spectroscopy (XPS) results (see below). The second species appears as structureless circular protrusion with a diameter of less than 8 Å. Its coverage observed by STM is considerably lower than that of AuTPP throughout the sample surface. It is plausible to attribute species 2 to chlorine and assume that a major fraction of the chlorine arriving at the surface is desorbed at room temperature. We note that the interaction of chlorine with Au(111) is strongly coverage dependent and controversially discussed in the literature.[17,18] The interpretation of the STM images is supported by our XPS results of mono- and multilayer films of $[Au^{III}TPP]^+Cl^-$ complementing the ultralow submonolayer STM samples. The photoemission spectra and respective binding energies are compiled in Figure 1d and Table 1, respectively. Figure 1d displays the XPS Au 4f region of monolayer samples. Since the Au 4f lines of the substrate are much stronger than the molecule related peaks, we subtracted the signal of the freshly cleaned substrate as obtained directly before evaporation the molecules. For this the substrate signal was scaled to take into account the damping by the organic layer. A doublet peak structure is observed with fitted binding energies of 88.4 and 91.7 eV (green). As expected, the Au 4f and Cl 2p binding energies of multilayer films on Au(111) are in agreement with literature values of $Au^{III}$ and $Cl^-$ ions listed in the bottom part of Table 1. The total intensity of the Au 4f doublet relative to the carbon signal (not shown) is consistent with the intensity expected for a homogeneous layer assuming that all molecules are in the $Au^{III}$ state. There is no significant change of the Au 4f binding energies between the multi- and monolayer, confirming that in the monolayer the high oxidation state of the central $Au^{III}$ ion is preserved. Moreover, no $Cl^-$ signal was detected for AuTPP monolayer coverage on Au(111), suggesting that $Cl^-$ separates from the AuTPP complex upon adsorption and partially desorbs upon AuTPP monolayer formation at room temperature. The remaining AuTPP species are stabilized as $[Au^{III}TPP]^+$ cations on the conducting template—consistent with the STM findings at ultralow coverage.

**TABLE 1. XPS Core-Level Binding Energies (eV) of Au 4f and Cl 2p for $[Au^{III}TPP]^+Cl^-$ Mono- and Multilayer Films on Au(111) and Literature Values**

| | | Au | | Cl | |
|---|---|---|---|---|---|
| | | $4f_{7/2}$ | $4f_{5/2}$ | $2p_{3/2}$ | ref |
| AuTPP (multi) | on Au(111) | 88.1 | 91.8 | 197.9 | |
| AuTPP (mono) | on Au(111) | 88.4 | 91.7 | NA[a] | |
| $Au^{III}$ | $NaAuCl_4$ | 87.4 | 91.1 | | 19 |
| | $Au(OH)_3$ | 87.7 | 91.4 | | 20 |
| | Au complex | 88 | 91.7 | | 21 |
| $Au^{I}$ | | 84.6 | | | 22 |
| | | 84.7 | | | 23 |
| $Au^0$ | solid Au | 83.9 | 87.6 | | 24 |
| $Cl^-$ | | | | 199.0 | 19 |
| | on Au surface | | | 197.0 | 19 |

[a] NA = not applicable.

**Substrate Effects on Frontier Orbitals.** In addition to stabilizing the active $Au^{III}$ state, the chemical accessibility of the frontier orbitals is mandatory for preserving the desired activity of the surface-supported agent molecules. Thus, identifying possible effects on the frontier MOs is cruical. LT-STM and scanning tunneling spectroscopy (STS) investigations of individual $[Au^{III}(TPP)]^+$ ions on Au(111) uncover the details of the frontier-orbital electronic structure. The tunneling spectrum of Figure 2a shows the energy-dependence of the local tunneling conductance under constant-current conditions with the tip positioned over the center of a single $[Au^{III}(TPP)]^+$ ion. An increased signal indicates resonant electron tunneling through specific electronic states of the adsorbate (states

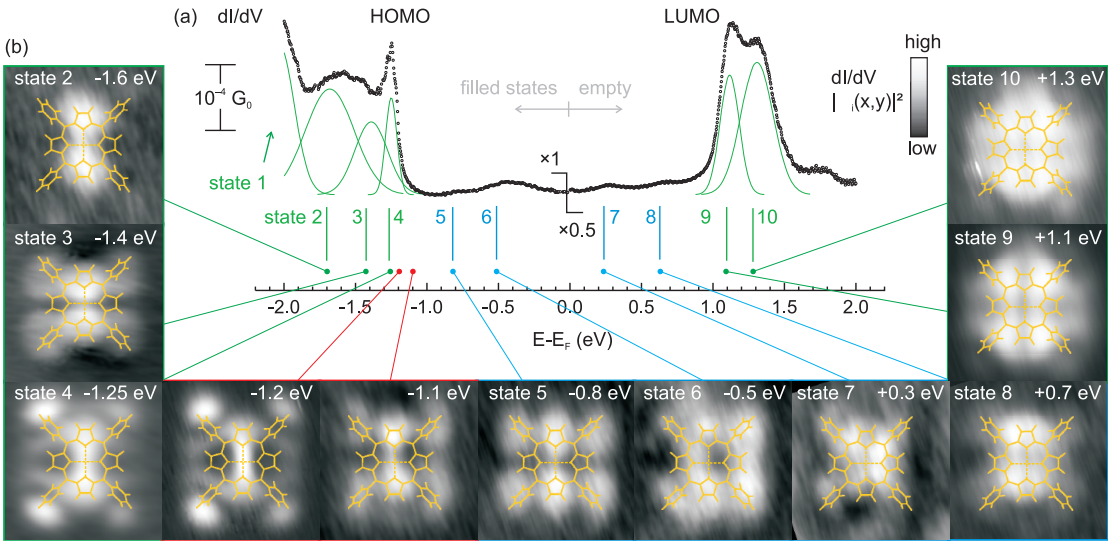


**Figure 2. (a) Experimental electron tunneling spectrum of single $[Au^{III}(TPP)]^+$ cations stabilized on a Au(111) surface recorded with the tip over the molecule center; $G_0 = 2e^2/h \approx 77.48\ \mu S$; multiple Gaussian peaks are fitted to the experimental data (green) indicating distinct states as listed in Table 2. (b) Imaging of MOs of single $[Au^{III}(TPP)]^+$: conductance maps (2.5 × 2.5 nm$^2$) obtained at different energies relative to the substrate Fermi level $E_F$; structural models of the molecular backbone are overlaid.**

**TABLE 2. Deconvolution of the Experimental Tunneling Spectrum of Figure 2b of a Single $[Au^{III}TPP]^+$ Ion on Au(111)[a]**

| state | energy (eV) | fwhm | assignment | DFT calculated orbital contributions |
|---|---|---|---|---|
| 1 | $< -2$ | | substrate | d (Au) |
| 2 | $-1.68 \pm 0.01$ | 0.40 | HOMO − 2 | $p_z$ (N, $C_{pyr}$) |
| 3 | $-1.39 \pm 0.01$ | 0.27 | HOMO − 1 | $p_z$ (N, $C_{pyr}$) |
| 4 | $-1.25 \pm 0.01$ | 0.1 | HOMO | $d_{z^2}$ ($Au^{III}$), $p_z$ (N, $C_{pyr}$, $C_{ph}$) |
| 5 | $-0.8 \pm 0.1$ | 0.35 | interface | $p_z$ ($C_{pyr}$, $C_{meso}$, N), $p_{x,y}$ ($C_{ph}$) |
| 6 | $-0.5$ | | Au(111) surface | |
| 7 | $+0.25 \pm 0.1$ | | substrate | d (Au) |
| 8 | $+0.65 \pm 0.1$ | | substrate | d (Au) |
| 9 | $+1.12 \pm 0.01$ | 0.16 | LUMO | $d_{x^2-y^2}$ ($Au^{III}$), $p_z$ ($C_{pyr}$, $C_{meso}$, N) |
| 10 | $+1.31 \pm 0.01$ | 0.26 | LUMO + 1 | $p_z$ ($C_{pyr}$, $C_{meso}$) |

[a] Electronic state energies and the full width at half maximum (fwhm) were obtained by a least-squares fit of the states 2−5, 9, and 10 by Gaussian peaks; all other energy and fwhm values are directly determined from the spectrum.

2−4, 9, 10), the substrate (states 1, 6−8) and the adsorbate/substrate interface (state 5). The resonant energies of the respective states are indicated by vertical bars in the spectrum. Table 2 summarizes the assignments of the electronic states and orbitals. Compared to the spectrum in ref 15, an additional sharp peak (state 4) is detected due to the optimized tunneling parameters of the present study as shown in Figure 2a. State 4 is centered at the low energy edge of the highest occupied molecular orbital (HOMO) indicating a significantly different electronic configuration of the adsorbed AuTPP compared to AuTPP in solution. In the latter case, the ligand-field split Au 5d-orbitals mix strongly to the LUMO of the complex but not the HOMO, similar to the gas-phase behavior.[15,25] Most strikingly, state 4 is exceptionally narrow, thus pointing to a weak coupling of the complex with molecular vibronic states[26] and electronic states of the substrate.[27,28] Figure 2b displays conductance maps (see Methods) recorded at the resonant energies of states 2−10. Each state is easily distinguished by its characteristic spatial conductance pattern. In the case of state 4 (at −1.25 eV), distinct changes are detected within a narrow energy range of only ±0.15 eV, where maximum conductance is measured directly over the center of the molecule (at −1.2 V in Figure 2). Obviously, state 4 has strong contributions of the $Au^{III}$ center ion as well as of pyrrole N and phenyl C atoms, in clear contrast to the neighboring states 3 and 5 where both exhibit nodal planes of reduced conductance through the center. Contrary to the HOMO, the Au-orbital mixing to the lowest unoccupied molecular orbial (LUMO, state 9) is only weakly affected by the adsorption process on Au(111). The respective conductance maps of Figure 2b indicate a nonzero mixing of $Au^{III}$ atomic orbitals to unoccupied MOs up to energies of at least +2 eV. The $Au^{III}$ ion mixes to both, HOMO and LUMO, which makes it chemically accessible in catalytic energy transfer processes. The conductance maps of states 2, 3, and 10 reveal that the pyrroles and meso carbons ($C_{meso}$) dominate the respective MOs. We remark that the effect of herringbone elbows on the d*I*/d*V* signature limits itself to a slight reduction of the HOMO−LUMO gap caused by asymmetric deformations of the molecule;[16] the MO mixing characteristics appears only weakly affected.

**Theoretical Analysis of Metal−Ligand Bonding.** The metal−ligand bonding is elucidated on an atomic scale by confronting the experimental results with first principles calculations of single $[Au^{III}(TPP)]^+$ ions on Au(111) [VASP code, see Methods]. Figure 3a presents the calculated density of states projected onto states of different

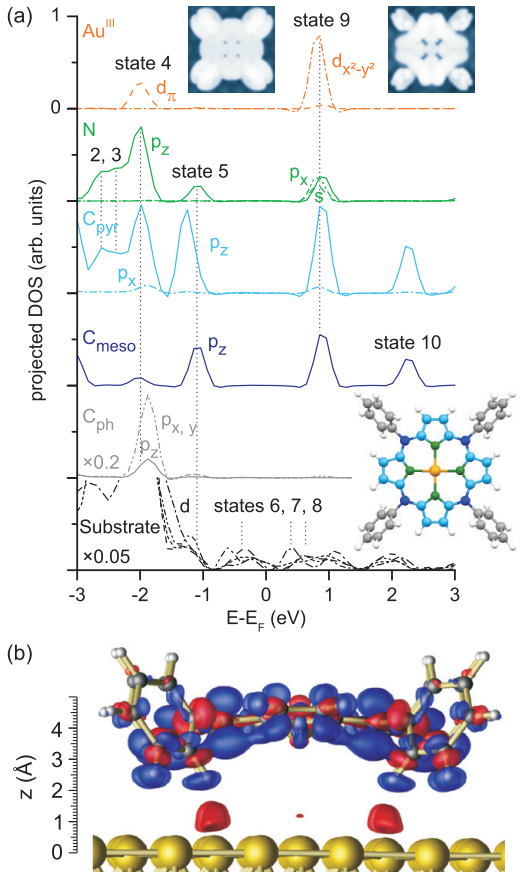


**Figure 3. DFT results of adsorbed $[Au^{III}(TPP)]^+$. (a) Calculated PDOS curves of different atomic groups displayed in separate colors (compare lower inset for color code); dotted vertical lines mark distinct states observed in conductance experiments (see text and compare Figure 2); (upper insets) constant-current Tersoff–Hamann STM simulation of a single $[Au^{III}(TPP)]^+$ on Au(111) at −2 V (left) and +0.9 V (right) bias voltage. (b) Side view of the DFT-calculated differential charge density of $[Au^{III}(TPP)]^+$ adsorbed on Au(111); red (blue) means a reduction (accumulation) of negative charge density compared to the isolated molecule in the gas phase.**

molecular units (PDOS) that contribute strongly to the MOs observed in the conductance maps of Figure 2b, that is, $Au^{III}$, N, $C_{meso}$, pyrrole C ($C_{pyr}$), and phenyl C ($C_{ph}$) as well as the substrate. Vertical dotted lines in Figure 3a mark the positions of respective STS states as indicated in Figure 2. Note that absolute energy values obtained by DFT may deviate by several 0.1 eV from experimental values.[29] The upper insets of Figure 3a show constant-current Tersoff–Hamann STM simulations of a single $[Au^{III}(TPP)]^+$ on Au(111) at energies of HOMO and LUMO obtained from our DFT results; they are consistent with experimental LT-STM images[15] as well as conductance maps of Figure 2b. The assignment of the calculated PDOS to STS states indicated in Figure 3 is based on a comparison with the most intense intramolecular units imaged in the conductance maps of Figure 1b. The contributing atomic orbitals are listed in the right column of Table 2.

In good agreement with experiment, the calculations reveal energetic resonance of the $Au^{III}$ $d_\pi$ orbitals ($d_{yz}$, $d_{zx}$ with $z$ components) with $p_z$ orbitals of N, $C_{pyr}$, and $C_{ph}$. In particular, the small spatial separation enables strong orbital intermixing of $Au^{III}$ and the pyrroles. Furthermore, a strong overlap of the $Au^{III}$ $d_{x^2-y^2}$ with orbitals of N, $C_{pyr}$, and $C_{meso}$ is indicated, all of them constituting the LUMO. Note that the $d_{x^2-y^2}$ orbital contribution appears less intense in the respective conductance map (state 9 in Figure 2), because the overlap between tip and sample wave functions is weak due to incompatible orbital symmetries. Note that in the case of pure W tips the surface state is $d_{z^2}$-derived,[30] while for Au-coated tips the Au surface state is sp-derived.[30,31] Although the $Au^{III}$ ion is energetically in resonance with extended d states of the substrate *via* the $d_\pi$ electrons of state 4, the overlap of the respective wave functions is weak because of its large vertical separation from the surface (~4.2 Å).[16] Also the covalent bonding between the porphyrin and the substrate is weak, involving only those parts of the phenyl groups that are closest to the surface [see differential charge density plot of Figure 3b]. A crystal orbital overlap population analysis of the $Au^{III}$–N bond confirms a weakly bonding character for HOMO and a stronger antibonding character for LUMO.

State 5 exhibits $p_z$ orbital contributions from the porphyrin (N, C) but not from $Au^{III}$ (note the scaling factor of 0.2 applied to the PDOS curve of $C_{ph}$). Its strongly involved molecular units, $C_{pyr}$ and $C_{ph}$, lie about 0.4–0.8 Å closer to the substrate than the $Au^{III}$–N core indicating coupling to electronic states of the substrate. Accordingly, state 5 is a mixed state. This is corroborated by the fact that the conductance map of state 5 strongly resembles that of state 6, which relates to the s–p-derived surface state of Au(111).[32] To obtain the surface state by the DFT calculation a much larger supercell would be required,[33] which was far beyond the available computing time. In contrast to state 5, a mixed interface state that strongly involves the central metal ion was reported for CoTPP.[27] A detailed analysis reveals that the onset of state 6 lies in the energy range where on the pristine Au(111) the surface state is observed. Since the latter is highly sensitive to coupling with other atomic or molecular states, the observed state 6 suggests that the coupling of electronic states of the adsorbed $[Au^{III}(TPP)]^+$ ion with the surface state is negligible in agreement with our DFT results. States 7 and 8 originate from the substrate as indicated by the absence of molecule contributions to the PDOS. The steep increase of $dI/dV$ below about −2 V is attributed to enhanced tunneling out of the substrate d band (state 1). In summary, the energetic resonances obtained with DFT calculations fit all states identified in the STS experiments and provide insight into the atomic orbitals contributing to the respective MOs.

**Image Charge Mimics Axial Ligand.** The square-planar tetracoordinate complexation with the four pyrroles of the porphyrin favors the $5d^8$ electronic configuration of $Au^{III}$.[34] A possible neutralization of $[Au^{III}(TPP)]^+$ *via* a one-electron transfer from the substrate necessitates the energetically unfavorable occupation of the LUMO. In the atomic orbital picture, this means the formation of a $Au^{II}$ state with $5d^9$ configuration, that is, an unpaired electron in the Au $5d_{x^2-y^2}$ orbital that contributes strongly to the (antibonding) LUMO. Instead, the positively charged state of AuTPP is stabilized similar to AuTPP in solution, where the $[Au^{III}(TPP)]^+$ cation is balanced by the negative countercharge of the chloride ions. This reasoning rationalizes the suppressed discharging of $[Au^{III}(TPP)]^+$ ions on the gold surface observed in the experiment, that is, the AuTPP moiety remains a cation upon adsorption. The latter implies a negative image charge in the substrate close to the interface that modifies the ligand field and, accordingly, affects the metal−ligand bonding interaction. Complementary to our VASP results (based on plane-wave functions), gas-phase DFT calculations with localized basis functions yield discrete MO levels as well as the linear combination of atomic orbitals (LCAO) coefficients, $c_i$. The latter enable a more detailed analysis of the image charge effect based on the identification of MOs with contributions from $Au^{III}$.

In the absence of a negative image charge, d orbitals are zero-field split by the square-planar tetracoordinate ligand field of the four porphyrine pyrroles, and each of them contributes to several different MOs of the AuTPP. The resulting intricate orbital mixing scheme can be simplified, in a first step, by analyzing only MOs with significant contributions of Au d orbitals with *z* component (the *i*th atomic-orbital contribution to a particular MO, *f*, is approximated by $f = c_i^2/\sum_j c_j^2$). The highest lying of these MOs (MO158) is about 1.6 eV below the HOMO (MO169) and has a strong Au $d_\pi$ contribution of $f(d_\pi) = 0.1$. Stronger Au $d_\pi$ contributions lie even lower in energy, namely about 4.5 eV and more below the HOMO and with $f(d_\pi)$ values up to ~0.3.

The presence of a negative image charge raises the potential energy of all MOs. In a series of model calculations the image charge effect is approximated by introducing a negative elementary point charge (−1*e*) located at variable distances in axial position to $[AuTPP]^+$. Figure 4a juxtaposes the respective energy shifts of exemplary MOs relative to the case with no point charge. Notably, the magnitude of the shift depends not only on the axial separation from the point charge, $\Delta z$, but also on the *z* component of the respective MO. The overall energy shift is determined by the Coulomb potential, $\Delta E_{pot} = (^1/_{4\pi\varepsilon_0})(e^2/\Delta z)$, plotted as a dotted curve in Figure 4a. A detailed analysis shows that MOs with strong *z* components exhibit larger shifts ($d_{z^2}$ and $d_\pi$, green curves) than MOs with dominant *x* or *y* components (blue curves), consistent with crystal field theory.

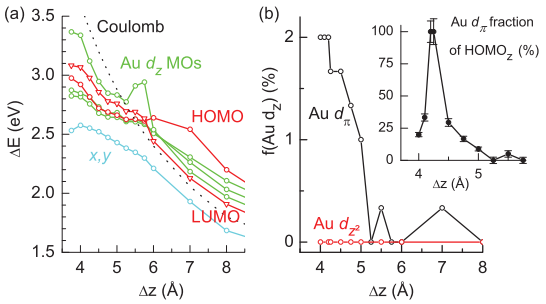


**Figure 4. Gas-phase DFT simulations of an electrostatic image charge model with a point charge of −1*e* in axial position to the $AuTPP^+$ complex acting as a negative countercharge. (a) Energy shifts, Δ*E*, of MOs with different *z* components as a function of the point-charge separation, Δ*z*, relative to isolated $AuTPP^+$; MOs with strong *z* components exhibit stronger shifts compared to MOs with dominant *x* and *y* components. (b) Distance-dependence of Au d orbital contributions to the HOMO with *z* components; (inset) Au $d_\pi$ contribution projected onto the *z* component of the HOMO.**

The enhanced upshift of atomic orbitals with *z* components by the Coulomb potential effectively increases their contributions to energetically higher lying MOs. A detailed analysis of the Au d orbital contributions to the HOMO (*f* values in %) reveals a strong increase of the $d_\pi$ fraction at axial separations smaller than 5 Å as illustrated in Figure 4b. The respective *f* values are obtained by summing orbital contributions over an energy range of ~0.7 eV below the HOMO (that is, including the three highest occupied MOs). We remark that a Mulliken population analysis[35] yields similar results. Near $\Delta z$ = 4 Å the $d_\pi$ fraction reaches a maximum of about 2%, while the $d_{z^2}$ fraction remains zero. The effect of $\Delta z$-dependent Au $d_\pi$ to the HOMO becomes even more striking, when the $d_\pi$ contribution is compared with the overall *z* component of the HOMO. The inset of Figure 4b shows that at $\Delta z \approx 4.2$ Å the full *z* component of the HOMO comes exclusively from the $d_\pi$ of the central Au ion and accounts for the sharp Au resonance observed by STM (Figure 2). Thus, the rather simple electrostatic model—treating the image charge *via* the *trans* effect[36] of a "fifth ligand"—yields an intriguingly good description of the STM and VASP results that indicate a Au d contribution of 5−10% to the HOMO (see Figure 2 and Figure 3). Furthermore, our simulations show that the STM tip as "sixth ligand" at a distance of >6 Å above the molecule does not significantly affect the presented experimental results (compare Figure 4b).

## CONCLUSIONS

Our combined experimental and theoretical study demonstrates that Au(111) facets are, indeed, a suitable template for functionalizing transferable nanoparticles as a therapeutic drug delivery system of cationic gold(III)-porphyrin derivatives. We uncover the exceptional adsorption behavior of individual $[Au^{III}(TPP)]^+$ adsorbed on Au(111), and provide a bonding scheme

explaining the origin of the $Au^{III}$-oxidation-state stabilization crucial for the medical functionality. The interaction of $[Au^{III}(TPP)]^+$ with the Au(111) surface is unique in several respects compared to that of other transition metal porphyrins: (1) Orbital overlap of the active $Au^{III}$ center and the substrate is weak, which is essential for preserving its specific catalytic properties; (2) the $Au^{III}$ d states mix considerably to both chemically relevant HOMO and LUMO; (3) a substantial image charge is induced in the metal substrate mimicking a "fifth ligand", which substitutes the role of the $Cl^-$ counterions in solution; (4) the latter facilitates the decisive upshift of Au $d_z$ orbitals to the HOMO. For an appropriate image potential, the Au d contribution to the chemically relevant frontier orbitals can be actively controlled *via* the *trans* effect. The observed exceptional adsorption mode is of general relevance for functionalizing nanocrystal facets with molecular agents that require the stabilization of a particular ionic state for a tailored catalytic activity.

## METHODS

The Au(111) surface was prepared by repeated cycles of 0.5 keV $Ar^+$ bombardment and annealing at 820 K. $[Au^{III}TPP]^+$ $Cl^-$ was thermally evaporated from a thoroughly degassed glass cruicible at a source temperature of 463 K and a pressure of less than $1 \times 10^{-9}$ mbar onto Au(111) held at 300 K.

STM experiments were performed at 7 K and a base pressure below $5 \times 10^{-11}$ mbar. W tips were electrochemically etched, vacuum-annealed above 1100 K, and subsequently Au-coated by controlled indentation into the pristine gold surface. The bias voltage, *V*, was applied to the sample. Compared to earlier work from our group,[15] the STS experiments were optimized by using two times larger tunneling currents and acquisition times and linearly decreasing the tunneling distance up to 50 pm with decreasing $|V|$. The set-point was +1 V, 30 pA, and *z*-offset $\leq$ 200 pm prior to deactivation of the feedback loop for recording the local differential tunneling conductance, d*I*/d*V*, with a sweep time of 120 s. The d*I*/d*V* signal was obtained with lock-in technique and a sinusoidal modulation peak-to-peak voltage of $V_{pp} = 20$ mV and 1 kHz added to *V*. Reliable judgment of the cleanliness and condition of our STM tips was based on routinely monitoring the d*I*/d*V* signature of the Au(111) surface state obtained over pure substrate regions and crosschecking its position and shape with literature values.[37] Conductance maps (spectroscopic images) were obtained by recording d*I*/d*V* point-by-point while scanning the molecule in constant-current mode.

XPS data were obtained with Al and Mg K$\alpha$ radiation and a hemispherical electron energy analyzer (100 mm radius) operated at a pass energy of 20 eV. The analyzer was equipped with a position sensitive resistive anode detector for increased sensitivity. The energy resolution of the setup of 1 eV was concluded from the width of the Ag 3d peaks. The energies were calibrated using the Au $4f_{7/2}$ and Au $4p_{1/2}$ reference binding energies of 83.9 and 642.7 eV, respectively. The recorded peak areas were consistent with the atomic percentage of the different elements in the Au-porphyrin taking into account the different scattering cross sections and the sensitivity of the analyzer.

The complete adsorbate has been calculated within a density functional theory (DFT) approach using the Vienna *ab Initio* Simulation Package (VASP)[38] and the PW91 functional[39] of the generalized gradient approximation to model the electron exchange and correlation. Owing to its large periodicity, the chevron reconstruction of the Au(111) surface[40] could not be modeled within our calculations.[16] The Au(111) surface is modeled using periodically repeated slabs with a nearly square surface supercell with $(8 \times 4)$ periodicity and four layers thickness separated by 25 Å vacuum. The topmost two layers and all atoms of the molecule were allowed to relax during optimization to replicate the atomic mismatch of the chevron elbows at the adsorption site upon adsorption of the $[AuTPP]^+$ complex. The electron-ion interaction is described by the projector-augmented wave (PAW) method.[41] For the Brillouin zone sampling, only the gamma point is used (energy cut off at 450 eV). The dispersive interactions not accounted for in DFT are modeled using a semiempirical London-type extension of the VASP code.[42] The charge of the molecular cation and the gold slab is determined by the total charge of the molecule−substrate system. We have compared total charges +1 and zero for which we obtained almost identical geometric and MO electronic structures. Herein, we relate to zero total charge of the molecule/substrate system.

Gas-phase DFT single point energy calculations were performed with the Gaussian 03 package[43] using Becke's three-parameter hybrid functional (B3LYP)[44] and fixed saddle-shape conformation of the AuTPP as obtained from our VASP calculations. A compound basis set was employed using Pople's 6-311+G(*d*,*p*) basis set for C, H, and N atoms, Los Alamos National Laboratory 2 (LANL2) relativistic effective core potentials[45] for the core electrons of the Au atom, and split-valence (double-$\zeta$) basis sets for the valence electrons of Au.

*Acknowledgment.* We acknowledge financial support by the Austrian Science Fund (FWF) (projects P20773 and P18384), the Deutsche Forschungsgemeinschaft, the ERC Advanced Grant MolART, and thank the Paderborn centre for Parallel Computing ($pc^2$) for computing time.

## REFERENCES AND NOTES

1. Kadish, K.; Smith, K.; Guilard, R. *The Porphyrin Handbook*; Academic Press: New York, 2003; Vol. 4, 11, 13.
2. Zhou, C. Y.; Chan, P. W. H.; Che, C. M. Gold(III) Porphyrin-Catalyzed Cycloisomerization of Allenones. *Org. Lett.* **2006**, *8*, 325–328.
3. Nijamudheen, A.; Jose, D.; Datta, A. Why Does Gold(III) Porphyrin Act as a Selective Catalyst in the Cycloisomerization of Allenones? *J. Phys. Chem. C* **2011**, *115*, 2187–2195.
4. Che, C.-M.; Sun, R. W.-Y.; Yu, W.-Y.; Ko, C.-B.; Zhu, N.; Sun, H. Gold(III) Porphyrins as a New Class of Anticancer Drugs: Cytotoxicity, DNA Binding, and Induction of Apoptosis in Human Cervix Epitheloid Cancer Cells. *Chem. Commun.* **2003**, 1718–1719.
5. Wang, Y.; He, Q. Y.; Sun, R. W. Y.; Che, C. M.; Chiu, J. F. Gold(III) Porphyrin 1a Induced Apoptosis by Mitochondrial Death Pathways Related to Reactive Oxygen Species. *Cancer Res.* **2005**, *65*, 11553–11564.
6. Sun, R.; Ma, D.; Wong, E.; Che, C. Some Uses of Transition Metal Complexes As Anticancer and Anti-HIV Agents. *Dalton Trans.* **2007**, 4884–4892.
7. Sun, R. W. Y.; Che, C. M. The Anticancer Properties of Gold(III) Compounds with Dianionic Porphyrin and Tetradentate Ligands. *Coord. Chem. Rev.* **2009**, *253*, 1682–1691.
8. Haeubl, M.; Reith, L. M.; Gruber, B.; Karner, U.; Müller, N.; Knör, G.; Schoefberger, W. DNA Interactions and Photocatalytic Strand Cleavage by Artificial Nucleases Based on Water-Soluble Gold(III) Porphyrins. *J. Biol. Inorg. Chem.* **2009**, *14*, 1037–1052.
9. Knör, G. Intramolecular Charge Transfer Excitation of Meso-Tetrakis(1-pyrenyl) Porphyrinato Gold(III) Acetate. Photosensitized Oxidation of Guanine. *Inorg. Chem. Commun.* **2001**, *4*, 160–163.

10. Katz, E.; Willner, I. Integrated Nanoparticle−Biomolecule Hybrid Systems: Synthesis, Properties, and Applications. *Angew. Chem., Int. Ed.* **2004**, *43*, 6042–6108.
11. Choi, C. H. J.; Alabi, C. A.; Webster, P.; Davis, M. E. Mechanism of Active Targeting in Solid Tumors with Transferrin-Containing Gold Nanoparticles. *Proc. Natl. Acad. Sci. U.S.A.* **2010**, *107*, 1235–1240.
12. Medintz, I. L.; Uyeda, H. T.; Goldman, E. R.; Mattoussi, H. Quantum Dot Bioconjugates for Imaging, Labelling and Sensing. *Nat. Mater.* **2005**, *4*, 435–446.
13. Kanehara, M.; Takahashi, H.; Teranishi, T. Gold(0) Porphyrins on Gold Nanoparticles. *Angew. Chem., Int. Ed.* **2008**, *47*, 307–310.
14. Lum, C. T.; Liu, X.; Sun, R. W.-Y.; Li, X.-P.; Peng, Y.; He, M.-L.; Kung, H. F.; Che, C.-M.; Lin, M. C. M. Gold(III) Porphyrin 1a Inhibited Nasopharyngeal Carcinoma Metastasis *in Vivo* and Inhibited Cell Migration and Invasion *in Vitro*. *Cancer Lett.* **2010**, *294*, 159–166.
15. Müllegger, S.; Schöfberger, W.; Rashidi, M.; Reith, L. M.; Koch, R. Spectroscopic STM Studies of Single Gold(III) Porphyrin Molecules. *J. Am. Chem. Soc.* **2009**, *131*, 17740–17741.
16. Müllegger, S.; Rashidi, M.; Lengauer, T.; Rauls, E.; Schmidt, W. G.; Knör, G.; Schöfberger, W.; Koch, R. Asymmetric Saddling of Single Porphyrin Molecules on Au(111). *Phys. Rev. B* **2011**, *83*, 165416.
17. Gao, W.; Baker, T. A.; Zhou, L.; Pinnaduwage, D. S.; Kaxiras, E.; Friend, C. M. Chlorine Adsorption on Au(111): Chlorine Overlayer or Surface Chloride? *J. Am. Chem. Soc.* **2008**, *130*, 3560–3565.
18. Zheleva, Z.; Dhanakb, V.; Held, G. Experimental Structure Determination of the Chemisorbed Overlayers of Chlorine and Iodine on Au111. *Phys. Chem. Chem. Phys.* **2010**, *12*, 10754–10758.
19. Kishi, K.; Ikeda, S. X-ray Photoelectron Spectroscopic Study of Reaction of Evaporated Metal-Films with Chlorine Gas. *J. Phys. Chem.* **1974**, *78*, 107–112.
20. Park, E.; Lee, J. Effects of Pretreatment Conditions on CO Oxidation over Supported Au Catalysts. *J. Catal.* **1999**, *186*, 1–11.
21. Criado, J. J.; Lopez-Arias, J. A.; Macias, B.; Fernandez-Lago, L. R.; Salas, J. M. Au(III) Complexes of Tris-Dithiocarbamate Derivatives of Alpha-Amino-Acids—Spectroscopic Studies, Thermal-Behavior, and Antibacterial Activity. *Inorg. Chim. Acta* **1992**, *193*, 229–235.
22. Fu, Q.; Saltsburg, H.; Flytzani-Stephanopoulos, M. Active Nonmetallic Au and Pt Species on Ceria-Based Water−Gas Shift Catalysts. *Science* **2003**, *301*, 935–938.
23. Matolin, V.; Cabala, M.; Matolinova, I.; Skoda, M.; Libra, J.; Vaclav, M.; Prince, K. C.; Skala, T.; Yoshikawa, H.; Yamashita, Y.; *et al*. $Au^{+}$ and $Au^{3+}$ Ions in $CeO_2$ RF-Sputtered Thin Films. *J. Phys. D: Appl. Phys.* **2009**, *42*, 11530.
24. Bearden, A.; Burr, A. F. Reevaluation of X-ray Atomic Energy Levels. *Rev. Mod. Phys* **1967**, *39*, 125.
25. Eng, M.; Ljungdahl, T.; Andreasson, J.; Martensson, J.; Albinsson, B. Triplet Photophysics of Gold(III) Porphyrins. *J. Phys. Chem. A* **2005**, *109*, 1776–1784.
26. Qiu, X. H.; Nazin, G. V.; Ho, W. Vibronic States in Single Molecule Electron Transport. *Phys. Rev. Lett.* **2004**, *92*, 206102.
27. Lukasczyk, T.; Flechtner, K.; Merte, L. R.; Jux, N.; Maier, F.; Gottfried, J. M.; Steinrück, H.-P. Interaction of Cobalt(II) Tetraarylporphyrins with a Ag(111) Surface Studied with Photoelectron Spectroscopy. *J. Chem. Phys. C* **2007**, *111*, 3090–3098.
28. Auwärter, W.; Seufert, K.; Klappenberger, F.; Reichert, J.; Weber-Bargioni, A.; Verdini, A.; Cvetko, D.; Dell'Angela, M.; Floreano, L.; Cossaro, A.; *et al.* Site-Specific Electronic and Geometric Interface Structure of Co-Tetraphenyl-Porphyrin Layers on Ag(111). *Phys. Rev. B* **2010**, *81*, 245403.
29. Jones, R. O.; Gunnarsson, O. The Density Functional Formalism, Its Applications and Prospects. *Rev. Mod. Phys.* **1989**, *61*, 689–746.
30. Chen, C. J. Tunneling Matrix Elements in Three-Dimensional Space: The Derivative Rule and the Sum Rule. *Phys. Rev. B* **1990**, *42*, 8841–8857.
31. Kevan, S. D.; Gaylord, R. H. High-Resolution Photoemission Study of the Electronic Structure of the Noble-Metal (111) Surfaces. *Phys. Rev. B* **1987**, *36*, 5809–5818.
32. Chen, W.; Madhavan, V.; Jamneala, T.; Crommie, M. Scanning Tunneling Microscopy Observation of an Electronic Superlattice at the Surface of Clean Gold. *Phys. Rev. Lett.* **1998**, *80*, 1469–1472.
33. Forster, F.; Bendounan, A.; Reinert, F.; Grigoryan, V. G.; Springborg, M. The Shockley-Type Surface State on Ar Covered Au(111): High Resolution Photoemission Results and the Description by Slab-Layer DFT Calculations. *Surf. Sci.* **2007**, *601*, 5595–5604.
34. Schmidbaur, H.; Cronje, S.; Djordjevic, B.; Schuster, O. Understanding Gold Chemistry through Relativity. *Chem. Phys.* **2005**, *311*, 151–161.
35. Mulliken, R. S. Electronic Population Analysis on LCAO-MO Molecular Wave Functions. I. *J. Chem. Phys. 23* **1955**, *23*, 1833–1840.
36. Coe, B. J.; Glenwright, S. J. *Trans* Effects in Octahedral Transition Metal Complexes. *Coord. Chem. Rev.* **2000**, *203*, 5–80.
37. Bürgi, L.; Brune, H.; Kern, K. Imaging of Electron Potential Landscapes on Au(111). *Phys. Rev. Lett.* **2002**, *89*, 176801.
38. Kresse, G.; Furthmueller, J. Efficiency of *ab-Initio* Total Energy Calculations for Metals and Semiconductors Using a Plane-Wave Basis Set. *Comput. Mater. Sci.* **1996**, *6*, 15.
39. Perdew, J. P.; Chevary, J. A.; Vosko, S. H.; Jackson, K. A.; Pederson, M. R.; Singh, D. J.; Fiolhais, C. Atoms, Molecules, Solids, and Surfaces: Applications of the Generalized Gradient Approximation for Exchange and Correlation. *Phys. Rev. B* **1992**, *46*, 6671–6687.
40. Barth, J. V.; Brune, H.; Ertl, G.; Behm, R. Scanning Tunneling Microscopy Observations on the Reconstructed Au(111) Surface—Atomic-Structure, Long-Range Superstructure, Rotational Domains and Surface Defects. *Phys. Rev. B* **1990**, *42*, 9307–9318.
41. Kresse, G.; Joubert, D. From Ultrasoft Pseudopotentials to the Projector Augmented-Wave Method. *Phys. Rev. B* **1999**, *59*, 1758–1775.
42. Ortmann, F.; Schmidt, W. G.; Bechstedt, F. Attracted by Long-Range Electron Correlation: Adenine on Graphite. *Phys. Rev. Lett.* **2005**, *95*, 186101.
43. Frisch, M. J.; Trucks, G. W.; Schlegel, H. B.; Scuseria, G. E.; Robb, M. A.; Cheeseman, J. R.; Montgomery, J. A.; Vreven, T.; Kudin, K. N.; Burant, J. C.*et al*. Gaussian 03, revision E.01. Gaussian, Inc.: Wallingford, CT, 2004.
44. Becke, A. D. Density-Functional Thermochemistry. III. The Role of Exact Exchange. *J. Chem. Phys.* **1993**, *98*, 5648.
45. Hay, P. J.; Wadt, W. R. *Ab Initio* Effective Core Potentials for Molecular Calculations—Potentials for K to Au Including the Outermost Core Orbitals. *J. Phys. Chem.* **1985**, *82*, 299–310.